HHS Public Access

Author manuscript

ACS Appl Mater Interfaces. Author manuscript; available in PMC 2019 April 10.

Published in final edited form as:

ACS Appl Mater Interfaces. 2018 December 12; 10(49): 42146–42154. doi:10.1021/acsami.8b17495.

Integrating 3D Printing and Biomimetic Mineralization for Personalized Enhanced Osteogenesis, Angiogenesis, and Osteointegration

Limin Ma[#†,‡,⊥], **Xiaolan Wang**[#†], **Naru Zhao**[#‡], **Ye Zhu**[§], **Zhiye Qiu**[∥], **Qingtao Li**[‡], **Ye Zhou**[⊥], **Zefeng Lin**[⊥], **Xiang Li**[#], **Xiaolong Zeng**[†], **Hong Xia**[⊥], **Shizhen Zhong**[¶], **Yu Zhang**[†], **Yingjun Wang**[‡], and **Chuanbin Mao**[§,△]

[†] Department of Orthopedics, Guangdong General Hospital, Guangdong Academy of Medical Sciences, Guangzhou, Guangdong 510080,PR China

[‡] School of Materials Science and Engineering, South China University of Technology, Guangzhou, 510641, PR China

[§] Department of Chemistry and Biochemistry, Stephenson Life Sciences Research Center, Institute for Biomedical Engineering, Science and Technology, University of Oklahoma, Norman, Oklahoma 73072, United States

Institute for Regenerative Medicine and Biomimetic Materials, Tsinghua University, Beijing 100084, PR China

[⊥] Department of Orthopedics, Guangdong Key Lab of Orthopedic Technology and Implant, Guangzhou General Hospital of Guangzhou Military Command, Guangzhou, 510010, PR China

[#] School of Mechanical Engineering, Shanghai Jiao Tong University, State Key Laboratory of Mechanical System and Vibration, Shanghai 200240, PR China

[¶] School of Basic Medical Sciences, Southern Medical University, Guangzhou 510515, PR China

[△] School of Materials Science and Engineering, Zhejiang University, Hangzhou, Zhejiang 310027, PR China

[#] These authors contributed equally to this work.

Abstract

Correspondence to: Yu Zhang; Yingjun Wang; Chuanbin Mao.

Supporting Information

The Supporting Information is available free of charge on the ACS Publications website at DOI: 10.1021/acsami.8b17495.

ASSOCIATED CONTENT

Primers used in PCR; mechanical properties of the PT, MC/PT2, and raduis; XRD patterns of PT and MC/ PT2; SEM images and EDS data of PT and MC/PT; high magnification FE-SEM images of PT and MC/PT2; flow cytometry analysis of rabbit BMSCs characterizations; hemolytic activity and visual observation of the PT, MC/PT1, MC/PT2, and MC/PT3; rabbit blood biochemical test of ALT, AST, GGT, Cr, UA, and urea; hematoxylin-eosin staining, as well as Masson's, trichrome staining of the MC/PT2 scaffold; vascularization of the MC/PT2 scaffold; and MC3T3-E1 cell proliferation and osteogenic differentiation on different scaffolds in vitro (PDF)

Notes

The authors declare no competing financial interest.

Titanium (Ti) alloy implants can repair bone defects at load-bearing sites. However, they mechanically mismatch with the natural bone and lack customized adaption with the irregularly major-sized load-bearing bone defects, resulting in the failure of implant fixation. Mineralized collagen (MC), a building block in bone, can induce angiogenesis and osteogenesis, and 3D printing technology can be employed to prepare scaffolds with an overall shape customized to the bone defect. Hence, we induced the formation of MC, made of hydroxyapatite (HAp) nanocrystals and collagen fibers, in 3D-printed porous Ti_6Al_4V (PT) scaffolds through in situ biomimetic mineralization. The resultant MC/PT scaffolds exhibited a bone-like Young's modulus and were customized to the anatomical contour of actual bone defects of rabbit model. We found that the biocompatibility and osteogenic differentiation are best when the mass ratio between HAp nanocrystals and collagen fibers is 1 in MC. We then implanted the MC/PT scaffolds into the customized radius defect rabbit model and found that the MC/PT scaffolds significantly improved the vascularized bone tissue formation and integration between new bone and the implants. Therefore, a combination of 3D printing and biomimetic mineralization could lead to customized 3D PT scaffolds for enhanced angiogenesis, osteogenesis, and osteointegration. Such scaffolds represent novel patient-specific implants for precisely repairing irregular major-sized load-bearing bone defects.

Graphical Abstract

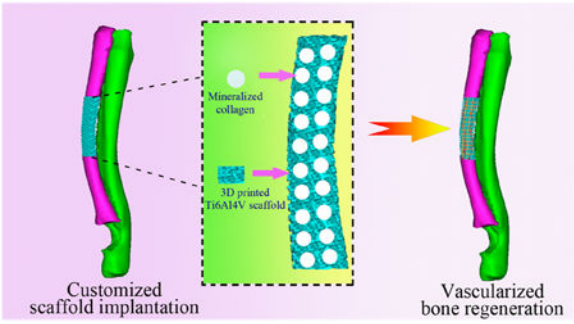

Keywords

porous titanium alloys; mineralized collagen; angiogenesis; osteogenesis; osteointegration

1. INTRODUCTION

Irregular large-sized load-bearing bone defects caused by trauma and tumor resection are a great challenge for clinicians.[1] Titanium (Ti) and the alloys based on it are widely used in orthopedics for repairing such defects because they have appropriate mechanical strength, good biocompatibility, and good corrosion tolerance.[2] But current Ti-based implants can cause stress-shielding because of mechanical mismatch and lack customized adaption with the actual bone defect, resulting in the failure of metallic Impalnt fixation.[3]The elasticity modulus of dense Ti is approximately 114 GPa, which was significantly greater than that of the trabecular and cortical bones (about 0.5 and 10–20 GPa, respectively), making it shield the stress of bone.[4–6] Porous scaffolds, fabricated by three-dimensional (3D) printing, might have decreased elastic modulus that potentially matches that of the bone tissue, and thus, 3D

printing is an effective approach to eliminating the mechanical mismatch between the scaffold and its neighboring tissue.[7] More importantly, to repair irregular bone defects with a complex 3D geometry, 3D printing can fabricate a patient-specific customized scaffold that perfectly fits the anatomical profile of such complex defects.[1] In addition, 3D printed scaffolds contain internal lattice structures, which can accommodate the new bone tissue to achieve excellent bone-implant integration.[8,9]

To develop customized scaffolds with bone-like mechanical properties for repairing complex bone defects, we first employed 3D printing to convert Ti_6Al_4V powder into porous titanium alloy (PT) scaffolds (Figure 1). To further enhance the bioactivity of the scaffolds, as well as the osteointegration with the scaffolds, we allowed the PT scaffolds to be modified with mineralized collagen (MC) matrix, which mimicked the bone matrix and thus could favor osteointegration.[10] The biomimetic MC matrix was formed on the scaffolds by immersing the scaffolds in a mineralizing solution containing collagen and hydroxyapatite (HAp) precursors. During the in situ biomimetic mineralization, the collagen fibrils were deposited on the scaffolds and mineralized by inducing HAp nanocrystals formation. MC matrix has a composition and microstructure resembling the native bone tissue compared to traditional artificial bone grafts.[11] Furthermore, it has been recently discovered that the MC matrix could more efficiently promote cell adhesion and proliferation as well as osteogenic differentiation than pure HAp, when mesenchymal stem cells (MSCs) isolated from bone marrow (BMSCs), were seeded on them.[12] The MC matrix could also induce bone regeneration and stimulate the growth of new blood vessels while being degraded via a creeping substitution process.[13] However, the MC matrix has poor mechanical strength, which could not be used in repairing major-sized load-bearing bone defects. Therefore, in this work we integrate 3D printing (to form patient-specific customized PT scaffolds) and biomimetic mineralization (to form the MC matrix) to form a new scaffold (MC/PT) that bears both bone-like mechanical properties and bone-inducing capabilities (Figure 1). We found that the scaffolds customized to a defect could facilitate BMSCs to differentiate into osteoblasts and repair bone defect successfully by inducing the angiogenesis and osteogenesis.

2. MATERIALS AND METHODS

2.1. Customized Design of Major-Sized Bone Defect Models.

The rabbit radius bone was scanned by microcomputed tomography (micro-CT). Computer-aided design (CAD) was utilized to establish a customized major-sized bone defect model (Figure 1A and B), and the model was saved as STL file format. Then, the CAD data were imported into a CAD software, employed to design the scaffolds with desired overall shape and interior pores, and then transferred to a 3D printer (Figure 1D).

2.2. Customized 3D Printed Porous Ti_6Al_4V Scaffold Fabrication.

Ti_6Al_4V powder (Sandvik, Sweden) with a diameter of 15–50 μm was printed into PT scaffolds using a Selective Laser Melting (SLM) 3D printer (Concept Laser M2, Upper Franconia, Germany). The 3D printer is equipped with an Yb-Faser-Laser with a focus beam diameter of 50 μm. The SLM processing occurred under an Ar/N_2 atmosphere using a laser

(100 W) with a set of scanning conditions (separation, 70 μm; rate, 650 mm/s; layer, 30 μm thick). After SLM processing, the scaffolds were removed from the 3D printer and cleaned ultrasonically in acetone and ethyl alcohol for 20 min to remove powders that were not melted during the SLM process.

2.3. Preparation of the Mineralized Collagen in Customized 3D Printed Porous Ti_6Al_4V Scaffolds.

Mineralized collagen (MC) was formed in the PT scaffolds to form MC/PT scaffolds, by following an in vitro biomimetic mineralization process.[14] First, collagen formed a viscous liquid by using dilute acetic acid to dissolve it, and calcium and phosphate salt solutions were added to the liquid. The mixed solution was then stirred to become homogeneous. The PT scaffolds were immersed into the mixed solution. Under the assistance of a vacuum pump, the mixed solution entered inner interconnected pore structure of the PT scaffolds. NaOH solution was dropped into the mixture to change its pH to 7 to trigger the formation of MC in the PT scaffolds (Figure 1E). The scaffolds were thoroughly washed, and finally freeze-dried to obtain the MC/PT scaffolds. The scaffolds were sterilized by ^{60}Co irradiation prior to use.

2.4. Characterization of Materials Structures and Phase Composition.

The porosity of the PT scaffolds ($n = 5$) was determined by quantifying their mass and volume. Mechanical properties of the scaffolds (5 mm wide, 6 mm high) were evaluated on an MTS 810 material testing system. The structures of the scaffolds were imaged using field-emission scanning electron microscopy (FE-SEM). Their elemental and phase composition were quantified by energy-dispersive X-ray spectroscopy (EDS) and X-ray diffraction (XRD), respectively. The XRD patterns were collected within the range of $2\theta = 0–90^{o}$ and using a step of 0.04° step and a scanning speed of 0.2 s/step.

2.5. Cell Purification and Culture.

BMSCs were isolated from New Zealand white rabbits (4-week-old). Briefly, the bone marrow, extracted under aseptic conditions, was centrifuged. Then, the pellet was suspended in a lymphocyte separation medium. After gradient centrifugation of the resultant suspension, BMSCs were purified and rinsed using a Hanks buffer (pH 7.2) twice. The cells were plated at a concentration of $5 \times 10^4/cm^2$ with low glucose Dulbecco's modified eagle medium (DMEM). The characterizations of rabbit BMSCs were performed by flow cytometry. Human umbilical vein endothelial cells (HUVECs, ATCC, USA) were incubated in an endothelial cell medium in an incubator. Both the cells and the medium used were from ScienCell (USA). The cells used in this study were at passages from 3 to 5.

2.6. Cell Attachment, Proliferation, and Viability.

BMSCs were seeded on the PT and MC/PT scaffolds (5×10^4 cells/cm^2). To confirm the cell attachment, the cells on the scaffolds were fixed, washed, sputter-coated with gold, and then imaged under SEM. The proliferation and viability of the BMSCs on the PT and MC/PT scaffolds were characterized using a cell counting kit-8 (CCK-8), following a reported protocol.[15]

2.7. Alkaline Phosphatase (ALP) Activity and Extracellular Matrix Mineralization.

The activity of an enzyme, ALP, was determined by following a reported protocol.[16] In addition, BCA protein assay was utilized to measure the content of the total intracellular protein, adopted to normalize the ALP activity, following the protocol of the vendor (Thermo Scientific, U.S.A.). Matrix mineralization of the BMSCs (1X 10^4 cells/mL) was assessed by carrying out Alizarin Red staining following our published protocol.[16]

2.8. Quantitative Real-Time PCR (RT-PCR) Analysis.

RT-PCR, using the primers listed in Tables S1 and S2 and glyceraldehyde-3- phosphate dehydrogenase (GAPDH) as a reference, was performed to evaluate the mRNA level of the genes related to osteogenesis and angiogenesis. After the BMSCs were cultured within the PT and MC/PT scaffolds for 7 and 14 days, the osteogenesis-related genes expressed by BMSCs including ALP, osteocalcin (OCN), type I collagen (Col-I), osteopontin (OPN), runt-related transcription factor 2 (Runx2) were confirmed by RT-PCR. The angiogenesis-related genes expressed by HUVECs included hypoxia-inducible factor α (HIFα), kinase insert domain-containing receptor (KDR), and vascular endothelial growth factor (VEGF). RT-PCR was performed after the HUVECs were cultured on the PT and MC/PT scaffolds for 3 and 10 days.

2.9. Animals and Surgical Procedures.

PT and MC/PT scaffolds were implanted into the middle of rabbit radius in vivo. New Zealand white rabbits (male and female, each with 12 rabbits) were divided randomly into 2 groups (weight ranged from 2.0 to 2.5 kg, $n = 12$). The animals were anesthetized by intravenous injection of a solution (3%) of phenobarbital sodium with a dose of 0.5 mL/kg. Muscle relaxant, xylazine hydrochloride, was applied for muscle relaxation at a dose of 0.1 mL/kg. An incision (~2.0 cm long) was generated to allow for the exposure of the middle of lateral radius. Then osteotomy was implemented to create a segmental bone defect in the middle of radius (about 1.5 cm in length along the longitudinal axis of radius). After meticulous hemostasis and hematocele clearing, a customized PT scaffold**,** which mimicked the anatomical contour of the removed bone segment, was then implanted to fill the defect. Cautious irrigation was taken before the incision was sutured. After the surgery, the animals were cared for in cages with free access to water and normal diet and observed regularly. This animal study received approvals from the Institutional Animal Care and Use Committee (IACUC) of Guangzhou General Hospital of Guangzhou Military Command.

2.10. Acute Hemolysis Assay and Biochemical Test.

Fresh anticoagulant whole blood from New Zealand White rabbits was diluted with physiological saline by a fold of 1.25. After the scaffolds were washed and then soaked in the saline, the soaking solution was refreshed with new saline (2 mL). The resultant mixture was then incubated in a water bath (37 °C) for half an hour, followed by the addition of dilute whole blood (0.2 mL). After 1 h, the suspension was subject to centrifugation at 3000 rpm for 5 min. Then a plate reader was employed to quantify the absorbance of the supernatant at 545 nm. In addition, two control samples were prepared. The positive one is the diluted whole blood (0.2 mL) mixed with distilled water (2 mL), and the negative one

was the physiological saline after treatment with the scaffolds as above. The hemolysis ratio (HR) was determined using the following equation and expressed as mean values (from three repeated experiments) of each group:

$$\mathrm{HR}(\%) = (O_S - O_N)/(O_P - O_N) \times 100 \quad (1)$$

where O_s, O_p, and O_N represented the average absorbance in the scaffold group, positive control group, and negative control group, respectively.

All rabbits were subject to blood samplings at preoperation and at weeks 4, and 12 postoperation using a vacutainer method with lithium heparin tubes. An automatic biochemical analyzer (Roche, module P800) was used to quantify aspartate aminotransferase (AST), gamma-glutamyl transpeptidase (GGT), alanine aminotransferase (ALT), uric acid (UA), creatinine (Cr), and urea.

2.11. Microcomputed Tomography (Micro-CT) Analysis.

The operation began when the rabbits were kept under anesthesia. After sacrifice of the animals, air was intravenously injected. After implantation for 4 and 12 weeks, the customized PT scaffolds were removed and scanned immediately through micro-CT to test the formation of new bone.[17] The scanning resolution is about 48 μm under 80 kV and 40 μA. The scanning matrix size was 1024 × 1024. The implantation area was continuously scanned to reach 500 layers. The bone volume percentage within a region of interest, termed BV/ TV, was determined using a software (VG Studio MAX).

2.12 Histopathological Analysis.

The tissue/scaffold constructs in each group were processed first into thicker sections (150 mm thick) by a microtome and then into thinner sections (~50 mm thick) by grinding and polishing. Soft-tissue in-growth and bone formation were characterized through hematoxylin and eosin (H&E) and Masson's trichrome staining.[18,19] The stained sections were then imaged by fluorescence microscopy.

2.13. Immunofluorescence Staining for Characterizing Vascularization.

Tissue slices were washed by PBS carefully and permeabilized using 0.5% Triton-100. They were blocked using 3% BSA for 1 h and allowed to interact with mouse primary antibody to CD31 (Abcam, ab199012, England) with a ratio of 1:100 to 1% BSA in PBS at 4 °C overnight. The slices were thoroughly washed by PBS, aged with Goat Anti-Mouse IgG (Alexa Fluor 647) (Abcam ab150115) with a ratio of 1:100 and thoroughly washed by PBS. In the end, Ul23DE3RFtraCruz Aqueous Mounting Medium with DAPI was added, and these images were observed and photographed by fluorescence microscopy.

3. RESULTS AND DISCUSSION

3.1. Mechanical Properties of the Scaffolds.

The density of solid Ti_6Al_4V was determined to be 4.42 g/cm3. The porosity of the PT scaffolds was found to be about 76.1% using a volume/weight analysis. By a compression test, we found that PT scaffolds with a porosity of 65%, 75%, and 85% had a magnitude stress of 105, 47, and 20 MPa, along with a Young's modulus of 4.15 ± 0.92, 1.60 ± 0.4, and 1.07 ± 0.29 GPa, respectively (Figure S1). The radius bone had a maximum compressive strength and modulus of 53 MPa and 1.81 ± 0.62 GPa, respectively (Figure S2). These data indicate that the PT scaffolds with a porosity of 65% and 75% had a better capability to bear loads. However, the Young's modulus of the PT group that had a porosity of 65% did not match that of rabbit radius (1.81 ± 0.62 GPa, Figure S2B). In addition, the PT scaffolds having a porosity of 85% had a maximum compressive strength of 20 MPa (Figure S1A), which was close to human cancellous bone[20] but was not good enough to bear loads. As for PT scaffolds with a 75% porosity, their modulus and maximum compressive strength (1.60 ± 0.4 GPa and 47 MPa, Figure S1) were similar to those of the radius and thus more suitable for repairing loading-bearing bone defects among the three levels of porosity (65%, 75%, and 85%). Therefore, the PT scaffolds with a porosity of 75% was chosen as the base scaffold for repairing load-bearing bone defects in this study. In addition, MC coating on the PT scaffolds was found not to modulate the mechanical properties of the PT scaffolds (Figure S3). Furthermore, according to the results from the scaffolds after bone regeneration for 3 months, there is no significant difference in the Young's modulus and ultimate strength between MC/PT2 (preoperative), MC/PT2 (postoperative), and rabbit radius (Figure S2).

3.2. Materials Characterization.

The phase composition of the deposited MC coating on the PT scaffolds was analyzed by XRD analyses (Figure S4). In PT scaffolds, the diffraction peaks of typical α and β Ti-based alloy phase were detected. With the MC addition, the diffraction peaks of HAp phase were also observed apart from the diffraction peaks of the Ti_6Al_4V matrix. Figures S5 and S6 showed the surface morphology and microstructure of the PT and MC/PT scaffolds. The PT scaffolds had a regular structure bearing pores with a size of about 400 μm.[21,22] The pores ofMC/PT1 (with a mineral/collagen mass ratio of 3:7) were blocked by MC (Figure S5C). However, the MC/PT2 scaffold with a mineral/collagen ratio of 5:5 was still porous and presented pores with a size of 100 to 400 μm (Figure S5E). The porous structure of MC/PT3 with a mineral/collagen ratio of 7:3 was also blocked by MC but showed a compact surface (Figure S5G). Energy dispersive spectroscopy (EDS) results showed that the elemental composition of PT mainly included Ti, Al, V, Fe, O, N, and C. Because MC/PT1, MC/PT2, and MC/ PT3 were all covered by MC, the elemental composition included C, N, O, P, Ca, Ti, and V. The calcium/phosphorus (Ca/P) molar ratio of MC/PT1, MC/PT2, and MC/PT3 was 1.53, 1.66 and 1.40, respectively, suggesting that the Ca/P ratio ofMC/PT2 was similar to the expected Ca/P value (1.67) of HA. The magnified area of the MC on the MC/PT2 scaffolds confirmed that the MC is indeed made of nanocrystalline HAp and collagen fibers (Figure S6).

3.3. Cell Identification, Morphology and Proliferation.

The cultured rabbit BMSCs were validated to be positive for CD29 and CD44 but negative for CD34 and CD45 by flow cytometry (Figure S7), confirming that these cells are indeed BMSCs. SEM micrographs demonstrated that BMSCs were attached to both the outer surfaces (Figure 2E-H) and inner surfaces (Figure 2D) of both PT and MC/PT scaffolds. More cells were found on the inner surfaces. BMSCs on the MC/ PT2 and MC/PT3 groups presented more lamellipodia extensions than those on the PT and MC/PT1 groups (Figure 2). We found that the cell proliferation increased over the time in the PT, MC/PT2, and MC/PT3 groups (Figure 2I). In addition, the PT and MC/PT1 groups presented a statistical difference in BMSCs proliferation, suggesting that MC/PT1 was cytotoxic. The results of cell morphology and proliferation (Figure 2) indicated that MC/PT1 had poor cell adhesion and cytotoxicity. Moreover, the MC was not well attached to the scaffolds in MC/PT1 (Figure S4). Hence, Figure 2 showed that MC/PT2 and MC/PT3 scaffolds promoted BMSCs cell proliferation, while MC/PT1 did not. Thus MC/PT1 scaffolds were excluded from the following studies.

3.4. ALP Activity, Extracellular Matrix Mineralization, and Quantitative RT-PCR Tests.

To identify the osteogenic differentiation on the PT, MC/PT2, and MC/PT3, the ALP activity and extracellular matrix mineralization assay were examined. ALP as an early osteogenic marker is important in mediating the osteogenic differentiation of BMSCs. On day 7, the MC/PT2 and MC/PT3 had a slightly high expression of ALP with no significant difference between them (Figure 3A). However, the MC/PT2 significantly enhanced the expression of ALP and MC/PT3 did not compared with PT on day 14, indicating that the addition of MC with a mineral/collagen ratio of 1:1 was beneficial to osteogenic differentiation of BMSCs.

Alizarin red staining was conducted to verify the mineralization (a late stage osteogenesis marker) on the scaffolds (Figure 3B). The relative absorbance value of the matrix mineralization cultured with MC/PT2 and MC/PT3 at 7 and 14 days was 130%, 109%, 131%, and 113%, in comparison with the PT group, respectively. The absorbance value due to the matrix mineralization of MC/PT2 was significantly greater than that of PT on both day 7 and 14. The results indicated that the addition of MC could promote extracellular matrix mineralization and thus the osteogenic differentiation.[23]

By RT-PCR, we found that the MC/PT2 group presented the highest level of the marker genes (OCN, ALP, OPN, Runx2, and Col-I) on days 7 and 14 (Figure 3C-G). These results showed that MC/PT2 induced osteogenic differentiation of BMSCs in vitro the best among all scaffolds. In addition, Figure 3C-G also indicated that MC/PT3, though not as good as MC/PT2, showed a better capability than PT in promoting the osteogenic differentiation. The addition of MC to the PT scaffolds with proper mineral content promoted the osteogenic differentiation is because MC, which is the most basic components in bone, is osteogenic. It has been consistently demonstrated that MC facilitates the BMSCs adhesion and osteogenic differentiation.[24–27]

Angiogenesis related genes are important for bone formation. Hence, we expected the MC/PT to promote both osteogenesis and angiogenesis. S. Yoshizawa et al. found that

hypoxia induction by HIFα expression facilitated the VEGF formation to promote bone angiogenesis.[28] It can be seen that MC/PT2 and MC/PT3 significantly promoted VEGF and HIFα gene expression by HUVECs as compared with PT on day 3 and 7 (Figure 3H-I). These results are consistent with the well-known role of MC in promoting angiogenesis by aiding the transcriptional activity of HIFα. Further results confirmed that MC/PT2 and MC/PT3 upregulated the gene expression of KDR compared with PT (Figure 3J). Collectively, these results confirm that the addition of MC to the PT scaffolds can up-regulate the VEGF gene expression in HUVECs through activating HIF-1a, resulting in enhanced angiogenesis.

3.5. Hemolysis Assay and Biochemical Test.

The blood compatibility of the scaffolds was investigated by hemolysis and biochemical analysis. By measuring hemoglobin release, the effect of scaffolds on the blood damage was quantified. The hemolysis rate of all scaffolds was less than 5% (Figure S8), showing that the scaffolds presented no hemolysis to red blood cells. In addition, no statistical differences were found in the levels of ALT, AST, GGT, Cr, UA, and urea in the blood after the PT and MC/PT2 scaffolds were implanted for different times (Figure S9), suggesting that the scaffolds did not induce toxicity in the live, kidney and blood.

3.6. Micro-CT, Histological Analysis, and Immunos-taining Analysis.

Since MC/PT2 showed the better BMSCs attachment, proliferation, and differentiation than MC/PT3, we chose MC/PT2 to conduct the animal experiment along with the PT as a control. We applied micro-CT to examine the ability of the scaffolds to promote osteogenesis. As the implantation time extended, both MC/PT2 and PT groups showed an increase in the volume ration between new bone and total tissue (denoted as BV/TV). Furthermore, the MC/ PT2 group presented a greater level of the BV/TV and BMD than the PT group for both week 4 and 12 (Figure 4E-F). These results showed that the MC/PT2 scaffolds presented a better capability in promoting bone regeneration than the PT scaffolds.

The osteogenesis and osteointegration guided by the MC/ PT2 scaffolds were assessed by H&E and Masson's trichrome staining. Trabeculae in the new bone (black arrows, Figure 5D) around the implants (white arrows, Figure 5D) in both PT and MC/PT2 groups became more regular and thicker on week 12 than those on week 4. Meanwhile, newly formed bone had thicker trabeculae in the MC/PT2 scaffold than in the PT scaffold at both time points (week 4 and 12). Furthermore, we found gaps between the new bone and PT scaffold on both week 4 and 12. But excellent integration between the new bone and scaffold was found in the MC/PT2 group. We also characterized the bone formation on the full tissue section slices by same staining on the MC/PT2 scaffolds 12 weeks postoperation (Figure S10). We found new bone both around and inside the implants. In addition, the results of the full views of implants cross section by immunofluorescence CD31 staining showed that mature vessels were formed around the implants (Figure S11). Taken together, integration ofMC with proper mineral/collagen ratio greatly enhanced the angio- genesis, osteogenesis, and osteointegration of the 3D-printed scaffolds. Moreover, we observed a significant increase cells (stained by DAPI) and vascular network (stained by CD31) in the PT and MC/PT2 over

the time (Figure 4G-J). A closer look at vascular network revealed more new vessels in the MC/PT scaffolds than in the PT scaffolds at the same time point (Figure 4G-J).

Once the supply of blood vessels is insufficient in bone tissue, metabolic, and oxygen demands will not be met, leading to the necrosis of central tissue.[9] Therefore, vascularization is particularly important to improve bone ingrowth and osseointegration.[29] Du et al. have shown that MC promotes angiogenesis in rat thigh muscle.[10] Hence, compared to the PT scaffolds, the MC/PT2 scaffolds promoted the vascularization, which further promoted bone formation (Figure 5). This result agrees with the earlier finding that MC could promote angiogenesis (Figure 4).

Among all MC-modified PT scaffolds, MC/PT2 with a mineral/collagen ratio of 5:5 showed the best capability in promoting cell proliferation and differentiation, suggesting the proper mineral/MC ratio is very important for controlling the cell behaviors. We also found that MC/PT2 facilitated the proliferation and osteogenesis of other precursor cells, such as MC3T3-E1 cells (Figure S12). These discoveries are consistent with the significantly improved performance of the MC/PT2 scaffolds in promoting osteointegration, osteogenesis, and vascularization compared to the PT scaffolds. This is expected as the natural bone components in the MC have been shown to promote the interactions between the implants and adjacent tissue,[30] as well as the osteoblast activities.[31] Overall, these results proved that the chemistry of the customized implants were important in directing the cell adhesion and proliferation as well as the cell differentiation.

Titanium alloy implants bearing excellent mechanical properties have been widely used in repairing major-sized load-bearing bone defects. However, they may cause stress- shielding due to mechanical mismatch and bone resorption, resulting in the implant failure. We found that the PT/MC2 scaffolds presented a trabecular bone-like Young’s modulus, indicating that the PT/MC2 scaffolds could decrease stress shielding (Figure S3). Because the complexity of bone defects and individual differences, an ideal bone repairing scaffold should match the anatomical structure of bone defects. Therefore, the 3D printing technology is perfect for fabricating a patient-specific customized implant with internal lattice structures that enhance osseointegration at the bone—implant junctions.[32] Osteointegration, osteogenesis and vascularization properties of bone repairing scaffolds are very important for their clinical applications.[33] Hence, the customized MC/PT2 scaffolds will find enormous potential in repairing bone defects at the load-bearing sites in a patient-specific manner. In addition, the customized 3D-printed scaffolds, once loaded with anticancer therapeutics,[34–38] could be potentially used as drug carrier for treating cancer.

4. CONCLUSION

In summary, we propose a novel method to increase the osteogenic potential and bone regenerative capability of a 3D printed Ti_6Al_4V scaffold customized to the actual defect in an animal model. Specifically, by biomimetic mineralization, MC was introduced to the surface of the scaffolds. We confirmed that because MC mimics the bone composition, addition of MC significantly promoted the osteogenesis, vascularization, and osteointegration of the 3D printed customized scaffolds. The scaffolds have a bone-like

Young's modulus and thus will mechanically match the bone. Thus, the MC-modified 3D printed customized Ti_6Al_4V scaffolds can be used to repair large bone defect in a load-bearing site in a patient-specific manner. Therefore, integration of 3D printing and biomimetic mineralization offers an effective strategy in precision medicine to repair major-sized bone defects by developing a new generation of patient-specific customized implants.

Supplementary Material

Refer to Web version on PubMed Central for supplementary material.

ACKNOWLEDGMENTS

This work was supported by National Key Research and Development Program of China (2016YFB0700803, 2017YFB0702604, 2016YFA0100900), National Natural Science Foundation of China (31700880, 31771038, 31600818, 51673168), Major International (Regional) Joint Research Project (21620102004), Scientific and Technological Project of Guangzhou, China (2018A030313709, 2015A030313608), Science and Technology Planning Project of Guangzhou city (201604020110, 201803010106), Military Logistic Science Research Project (BGZ15J001). Y.Z. and C.M. thank National Institutes of Health (EB021339) for financial support.

REFERENCES

(1). Xiu P; Jia Z; Lv J; Yin C; Cheng Y; Zhang K; Song C; Leng H; Zheng Y; Cai H; et al. Tailored Surface Treatment of 3D Printed Porous Ti_6Al_4V by Micro-Arc Oxidation for Enhanced Osseointegration via Optimized Bone In-Growth Patterns and Interlocked Bone/Implant Interface. ACS Appl. Mater. Interfaces 2016, 8, 17964–17975. [PubMed: 27341499]

(2). Mei S; Wang H; Wang W; Tong L; Pan H; Ruan C; Ma Q; Liu M; Yang H; Zhang L; et al. Antibacterial Effects and Biocompatibility of Titanium Surfaces with Graded Silver Incorporation in Titania Nanotubes. Biomaterials 2014, 35, 4255–4265. [PubMed: 24565524]

(3). Arabnejad S; Johnston B; Tanzer M; Pasini D Fully Porous 3D Printed Titanium Femoral Stem to Reduce Stress-Shielding Following Total Hip Arthroplasty. J. Orthop. Res. 2017, 35, 1774–1783. [PubMed: 27664796]

(4). Parthasarathy J; Starly B; Raman S; Christensen A Mechanical Evaluation of Porous Titanium (Ti_6Al_4V) Structures With Electron Beam Melting (EBM). J. Mech. Behav. Biomed. Mater. 2010, 3, 249–259. [PubMed: 20142109]

(5). Ryan G; Pandit A; Apatsidis DP Fabrication Methods of Porous Metals for Use in Orthopaedic Applications. Biomaterials 2006, 27, 2651–2670. [PubMed: 16423390]

(6). Arabnejad S; Johnston B; Tanzer M; Pasini D Fully Porous 3D Printed Titanium Femoral Stem to Reduce Stress-Shielding Following Total Hip Arthroplasty. J. Orthop. Res. 2017, 35, 1774–1783. [PubMed: 27664796]

(7). Li G; Wang L; Pan W; Yang F; Jiang W; Wu X; Kong X; Dai K; Hao Y In vitro and In Vivo Study of Additive Manufactured Porous Ti_6Al_4V Scaffolds for Repairing Bone Defects. Sci. Rep. 2016, 6, 34072. [PubMed: 27667204]

(8). Shah FA; Omar O; Suska F; Snis A; Matic A; Emanuelsson L; Norlindh B; Lausmaa J; Thomsen P; Palmquist A Long-Term Osseointegration of 3D Printed CoCr Constructs with an Interconnected Open-Pore Architecture Prepared by Electron Beam Melting. Acta Biomater. 2016, 36, 296–309. [PubMed: 27000553]

(9). Wang J; Yang M; Zhu Y; Wang L; Tomsia AP; Mao CB Phage Nanofibers Induce Vascularized Osteogenesis in 3D Printed Bone Scaffolds. Adv. Mater. 2014, 26, 4961–4966. [PubMed: 24711251]

(10). Jing Z; Wu Y; Su W; Tian M; Jiang W; Cao L; Zhao L; Zhao Z Carbon Nanotube Reinforced Collagen/Hydroxyapatite Scaffolds Improve Bone Tissue Formation In Vitro and In Vivo. Ann. Biomed. Eng. 2017, 45, 2075. [PubMed: 28620768]

(11). Liu Y; Luo D; Kou XX; Wang XD; Tay FR; Sha YL; Gan YH; Zhou YH Hierarchical Intrafibrillar Nanocarbonated Apatite Assembly Improves the Nanomechanics and Cytocompatibility of Mineralized Collagen. Adv. Funct. Mater. 2013, 23, 1404–1411.

(12). Xu SJ; Qiu ZY; Wu JJ; Kong XD; Weng XS; Cui FZ; Wang XM Osteogenic Differentiation Gene Expression Profiling of hMSCs on Hydroxyapatite and Mineralized Collagen. Tissue Eng, Part A 2016, 22, 170–181.

(13). Liao SS; Cui FZ; Zhang W; Feng QL Hierarchically Biomimetic Bone Scaffold Materials: Nano-HA/collagen/PLA Composite. J. Biomed. Mater. Res. 2004, 69B, 158–165.

(14). Zhang W; Liao SS; Cui FZ Hierarchical Self-Assembly of Nano-Fibrils in Mineralized Collagen. Chem. Mater. 2003, 15, 3221–3226.

(15). Park J; Lee J; Kwag J; Baek Y; Kim B; Yoon CJ; Bok S; Cho SH; Kim KH; Ahn G; et al. Quantum Dots in an Amphiphilic Polyethyleneimine Derivative Platform for Cellular Labeling, Targeting, Gene Delivery, and Ratiometric Oxygen Sensing. ACS Nano 2015, 9, 6511–6521. [PubMed: 26057729]

(16). Ning C; Yu P; Zhu Y; Yao M; Zhu X; Wang X; Lin Z; Li W; Wang S; Tan G; Zhang Y; Wang Y; Mao CB Built-in Microscale Electrostatic Fields Induced by Anatase-Rutile-Phase Transition in Selective Areas Promote Osteogenesis. NPG Asia Mater. 2016, 8, e243. [PubMed: 27818718]

(17). Jones AC; Arns CH; Sheppard AP; Hutmacher DW; Milthorpe BK; Knackstedt MA Assessment of Bone Ingrowth into Porous Biomaterials Using Micro-CT. Biomaterials 2007, 28, 2491–2504. [PubMed: 17335896]

(18). Park JK; Shim JH; Kang KS; Yeom J; Jung HS; Kim JY; Lee KH; Kim TH; Kim SY; Cho DW; et al. Solid FreeForm Fabrication of Tissue-Engineering Scaffolds with a Poly(lactic- co-glycolic acid) Grafted Hyaluronic Acid Conjugate Encapsulating an Intact Bone Morphogenetic Protein-2/Poly(ethylene glycol) Complex. Adv. Funct. Mater. 2011, 21, 2906–2912.

(19). Yang M; Shuai Y; Sunderland KS; Mao C Ice-templated Protein Nanoridges Induce Bone Tissue Formation. Adv. Funct. Mater. 2017, 27, 1703726. [PubMed: 29657571]

(20). Kokubo T; Kim HM; Kawashita M Novel bioactive materials with different mechanical properties. Biomaterials 2003, 24, 2161–2175. [PubMed: 12699652]

(21). Bai F; Wang Z; Lu J; Liu J; Chen G; Lv R; Wang J; Lin K; Zhang J; Huang X The Correlation Between the Internal Structure and Vascularization of Controllable Porous.Bioceramic Materials In Vivo: A Quantitative Study. Tissue Eng, Part A 2010, 16, 3791–3803.

(22). Wang X; Xu S; Zhou S; Xu W; Leary M; Choong P; Qian M; Brandt M; Xie YM Topological design and additive manufacturing of porous metals for bone scaffolds and orthopaedic implants: A review. Biomaterials 2016, 83, 127–141. [PubMed: 26773669]

(23). Tan F; O'Neill F; Naciri M; Dowling D; Alrubeai M Cellular and Transcriptomic Analysis of Human Mesenchymal Stem Cell Response to Plasma-Activated Hydroxyapatite Coating. Acta Biomater. 2012, 8, 1627–1638. [PubMed: 22202907]

(24). Wang QQ; Li W; Yang BC Regulation on the Biocompatibility of Bioactive Titanium Metals by Type I Collagen. J. Biomed. Mater. Res. Part A 2011, 99A, 125–134.

(25). Ma XY; Feng YF; Ma ZS; Li X; Wang J; Wang L; Lei W The Promotion of Osteointegration Under Diabetic Conditions Using Chitosan/Hydroxyapatite Composite Coating on Porous Titanium Surfaces. Biomaterials 2014, 35, 7259–7270. [PubMed: 24912815]

(26). Yang M; Wang J; Zhu Y; Mao C Bio-Templated Growth of Bone Minerals from Modified Simulated Body Fluid on Nanofibrous Decellularized Natural Tissues. J. Biomed. Nanotechnol 2016, 12, 753–761. [PubMed: 27301201]

(27). Yang M; Zhou G; Castanoizquierdo H; Zhu Y; Mao C Biomineralization of Natural Collagenous Nanofibrous Membranes and Their Potential Use in Bone Tissue Engineering. J. Biomed. Nanotechnol. 2015, 11, 447–456. [PubMed: 25883539]

(28). Yoshizawa S; Brown A; Barchowsky A; Sfeir C Magnesium Ion Stimulation of Bone Marrow Stromal Cells Enhances Osteogenic Activity, Simulating the Effect of Magnesium Alloy Degradation. Acta Biomater. 2014, 10, 2834–2842. [PubMed: 24512978]

(29). Liu H; Li W; Liu C; Tan J; Wang H; Hai B; Cai H; Leng HJ; Liu ZJ; Song CL Incorporating Simvastatin/ Poloxamer 407 Hydrogel into 3D-printed Porous Ti_6Al_4V Scaffolds for the

Promotion of Angiogenesis, Osseointegration and Bone Ingrowth. Biofabrication 2016, 8, 045012. [PubMed: 27788122]

(30). Wang Z; Chen L; Wang Y; Chen X; Zhang P Improved Cell Adhesion and Osteogenesis of op-HA/PLGA Composite by Poly(dopamine)-Assisted Immobilization of Collagen Mimetic Peptide and Osteogenic Growth Peptide. ACS Appl. Mater. Interfaces 2016 8, 26559–26569. [PubMed: 27649958]

(31). Xia Z; Yu X; Wei M Biomimetic Collagen/Apatite Coating Formation on Ti_6Al_4V Substrates. J. Biomed. Mater. Res. Part B 2012, 100B, 871–881.

(32). Wong KC; Kumta SM; Geel NV; Demol J One-Step Reconstruction with a 3D-Printed, Biomechanically Evaluated Custom Implant After Complex Pelvic Tumor Resection. Comput. Aided Surg. 2015, 20, 14–23. [PubMed: 26290317]

(33). Li Y; Yang W; Li X; Zhang X; Wang C; Meng X; Pei Y; Fan X; Lan P; Wang C; et al. Improving Osteointegration and Osteogenesis of Three-Dimensional Porous Ti_6Al_4V Scaffolds By Polydopamine-Assisted Biomimetic Hydroxyapatite Coating. ACS Appl. Mater. Interfaces 2015, 7, 5715–5724. [PubMed: 25711714]

(34). Kalarical Janardhanan S; Narayan S; Abbineni G; Hayhurst A; Mao C Architectonics of phage-liposome nanowebs as optimized photosensitizer vehicles for photodynamic cancer therapy. Mol. Cancer Ther. 2010, 9, 2524–2535. [PubMed: 20807781]

(35). Gandra N; Abbineni G; Qu X; Huai Y; Wang L; Mao C Bacteriophage bionanowire as a carrier for both cancer-targeting peptides and photosensitizers and its use in selective cancer cell killing by photodynamic therapy. Small 2013, 9, 215–221. [PubMed: 23047655]

(36). Ngweniform P; Abbineni G; Cao B; Mao C Self-assembly of drug-loaded liposomes on genetically engineered target-recognizing M13 phage: a novel nanocarrier for targeted drug delivery. Small 2009, 5, 1963–1969. [PubMed: 19415651]

(37). Jiang L; Lan R; Huang T; Chan C; Li H; Lear S; Zong J; Wong W; Muk-Lan Lee M; Dow Chan B; Chan W; Lo W; Mak N; Li Lung M; Lok Lung H; Wah Tsao S; Taylor G; Bian Z; Tai W; Law G; Wong W; Cobb S; Wong K EBNA1-targeted probe for the imaging and growth inhibition of tumours associated with the Epstein-Barr virus. Nat. Biomedical. Eng. 2017, 1, 0042.

(38). Zhou Y; Chan C; Kwong D; Law G; Cobb S; Wong W; Wong K $\alpha v\beta 3$-Isoform specific erbium complexes highly specific for bladder cancer imaging and photodynamic therapy. Chem. Commun. 2017, 53, 557–560.

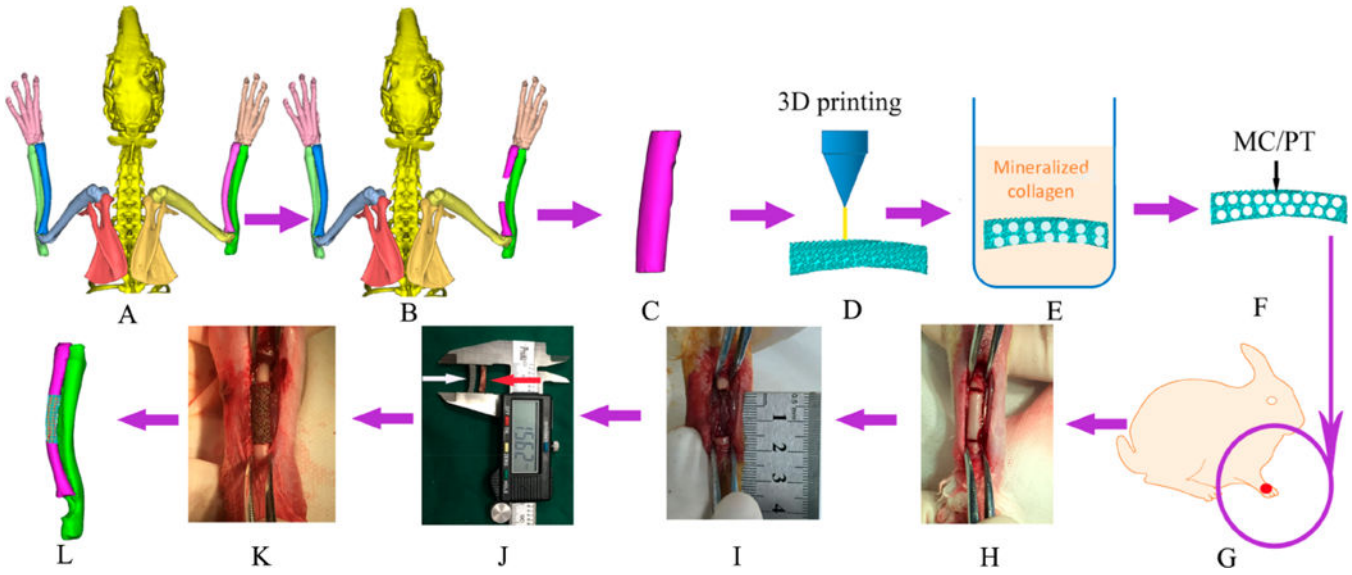

Figure 1.

Schematic of the overall idea. (A, B) A segmental bone defect (B) was formed in the middle of lateral radius of the healthy rabbit (A), as confirmed by micro-CT scanning. (C, D) On the basis of the micro-CT image of the bone defect (B) and by computer-aided design, a bone tissue model (C) fitting the profile of actual defect (B)was designed and reconstructed into a customized porous Ti_6Al_4V scaffold by 3D printing (D). (E-G) The porous 3D printed Ti_6Al_4V customized scaffold (termed PT) was filled with mineralized collagen (MC) by in situ mineralization to form a new scaffold (termed MC/PT) (E, F). PT and MC/PT were implanted into the middle of lateral radius (G). (H, I) To generate the bone defect, bone with about 1.5 cm in length along the longitudinal axis of radius was cut (H) and then taken out to form a defect (I). (J-L) To evaluate the scaffolds in repairing bone defect, the MC/PT scaffold (white arrow) was compared to the bone taken out of the animal to confirm that they have similar size and shape (J), then the MC/PT scaffold was implanted into the defect (K), and finally new bone and blood vessel were grown into the scaffold to achieve bone defect repair (L).

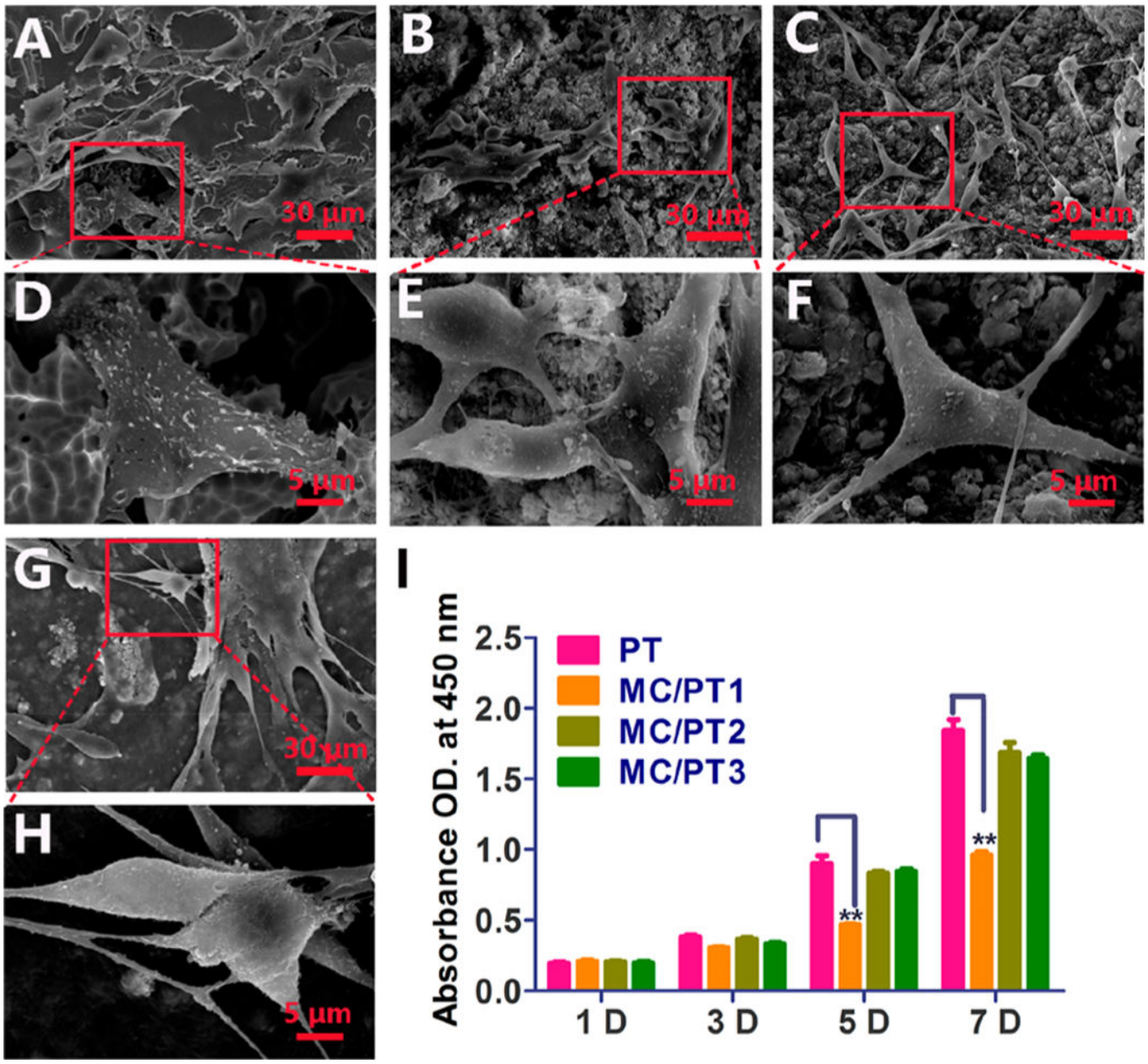

Figure 2.

BMSCs morphology and proliferation on different scaffolds. (A-H) SEM graphs of cells cultured on PT (A and D), MC/PT1 (B and E), MC/PT2 (C and F), and MC/PT3 (G and H) scaffolds for 24 h. (I) BMSCs proliferation by CCK-8 assay after different times (1, 3, 5, and 7 days of incubation). ** $p < 0.01$ (compared to the PT group).

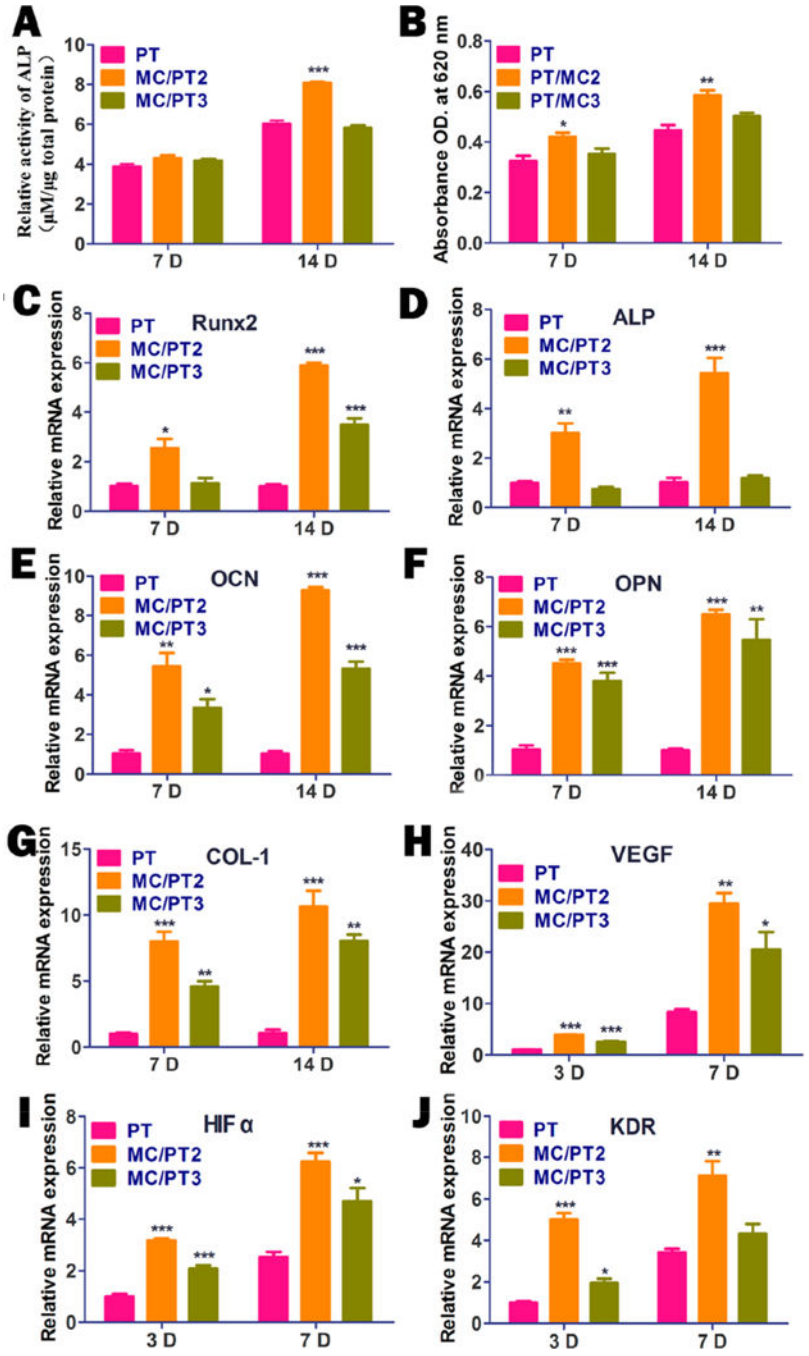

Figure 3.

Analysis of osteogenic differentiation and angiogenesis on different scaffolds in vitro. (A, B) The osteogenic differentiation on the scaffolds evaluated on days 7 and 14 by assaying ALP activity (A) and extracellular matrix mineralization (B). (C-G) Osteogenic related gene expressions of RunX2 (C), ALP (D), OCN (E), OPN (F), and Col-I (G) by the cells cultured with PT, MC/PT2, and MC/ PT3 for different times (7 and 14 days). (H-J) Expression of angiogenesis-related genes including VEGF (H), HIFα (I), and KDR (J) by HUVECs

cultured with PT, MC/PT2, and MC/PT3 for different times (3 and 7 days). *$p < 0.05$, * *$p < 0.01$, and ***$p < 0.001$ compared with PT.

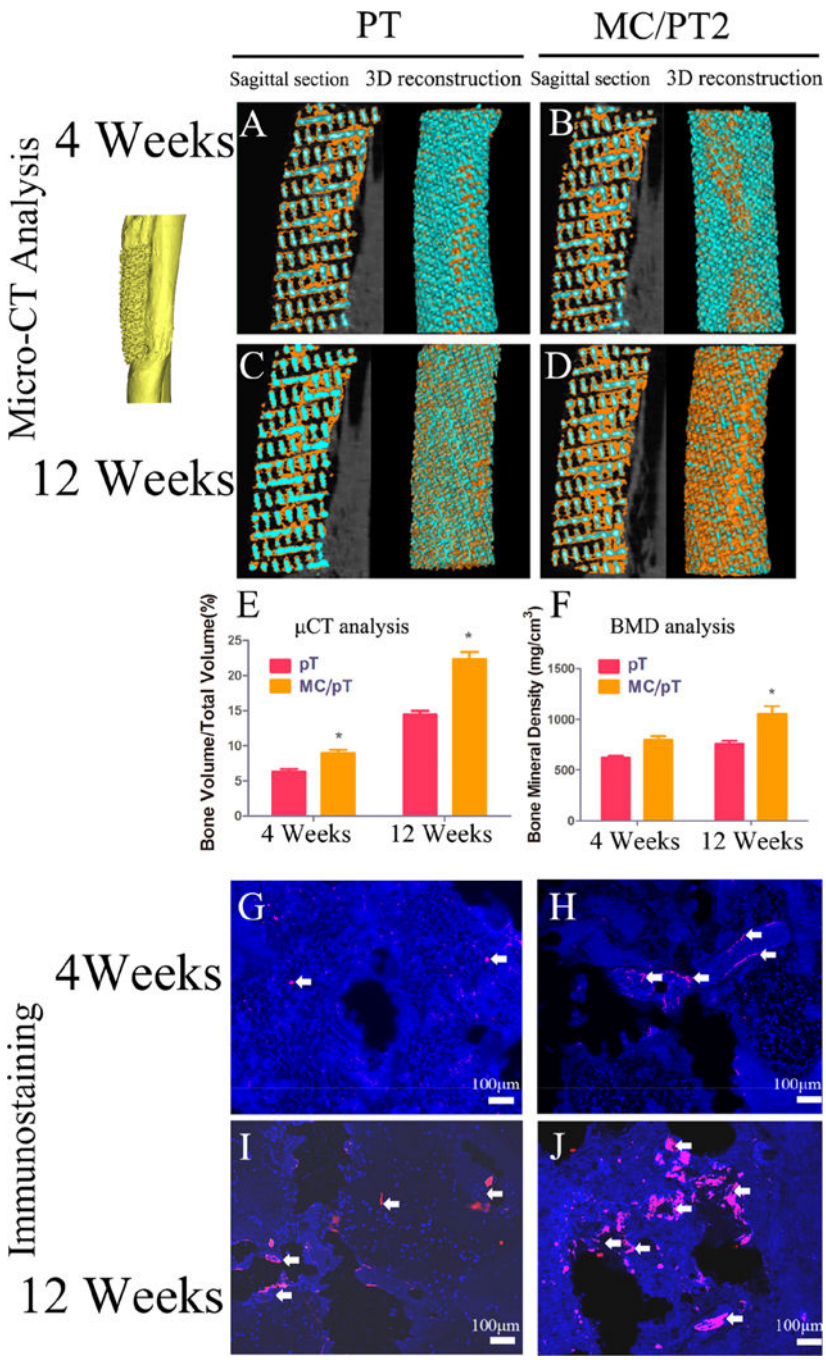

Figure 4.

Osseointegration and vascularization around the PT and MC/PT2 scaffolds. (A-D) Sagittal section and 3D reconstruction of the PT and MC/PT2 scaffolds after 4 and 12 weeks of in vivo experiment (orange represented new bone in 3D micro-CT images). (E-F) Volume percentages of bone in tissue (BV/TV), as well as bone mineral density (BMD) (F) in the PT and MC/PT2 scaffolds. $*p < 0.05$ (compared to the PT scaffold). (G-J) Immunofluorescence CD31 staining showed that the mineralized collagen facilitated vessel maturation in the PT

and MC/PT2 scaffolds. (blue, DAPI; red, CD31; white arrows, cells with CD31 positive expression).

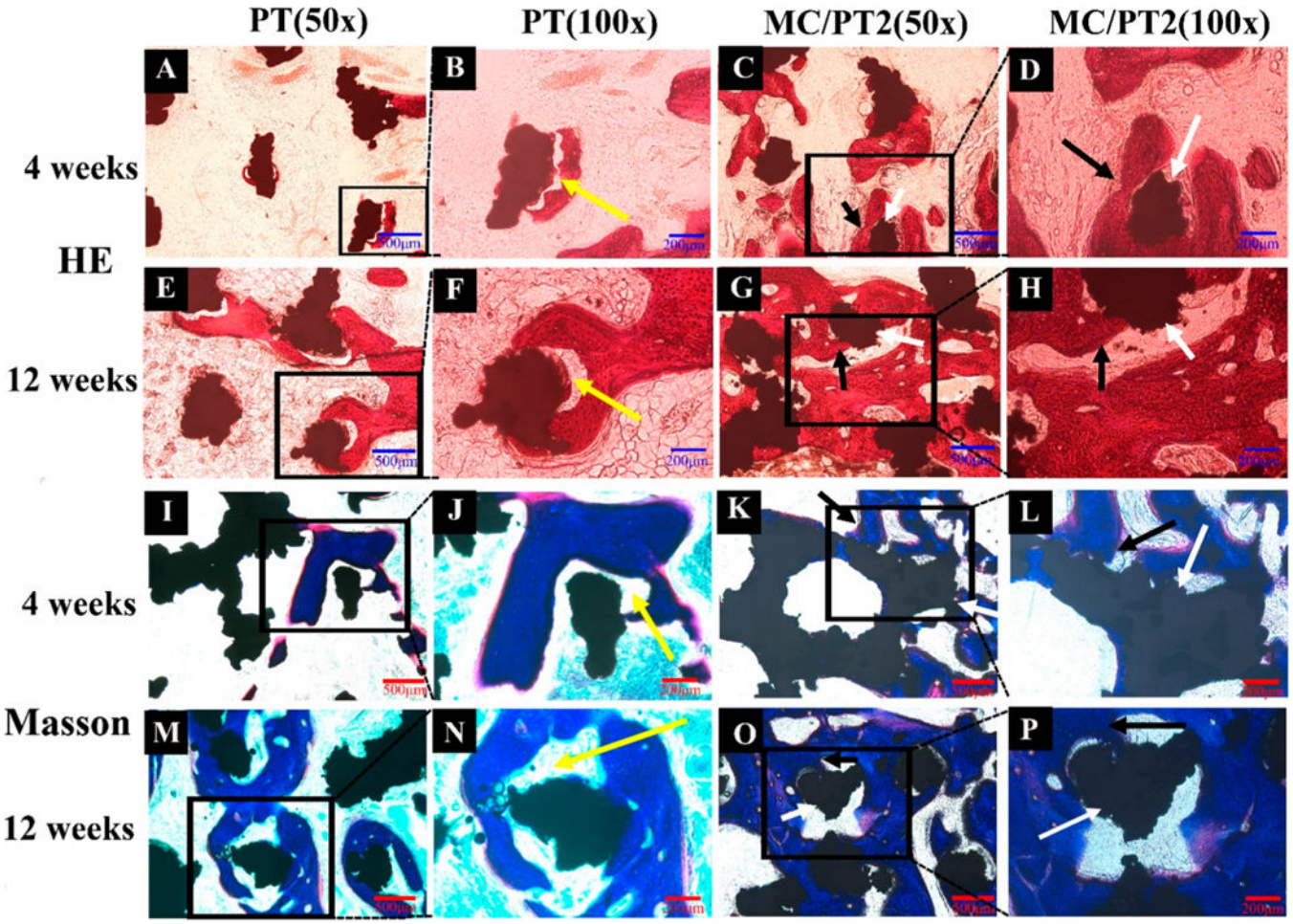

Figure 5.

In vivo osteogenesis on different scaffolds. H&E staining (A-H) and Masson's trichrome staining (I-P) of the PT and MC/PT2 scaffolds 4 and 12 weeks after operation were conducted to identify bone regeneration. Trabeculae of new bone (denoted by black arrows) were found around the implants (white arrows). The tissue (red-stained in HE staining, A—H; blue-stained in Masson staining, I—P) represented the new bone. The MC/PT2 group presented thicker trabeculae than the PT group on both week 4 and 12. Gaps (yellow arrows) were found at the new bone/implant boundary in the PT group on both week 4 and 12. The results demonstrated that MC in the PT scaffolds greatly facilitated the osteogenesis and osteointegration.